

Energy relaxation properties of a microwave resonator coupled to a pumped two-level system bath

Thibault Capelle,¹ Emmanuel Flurin,² Edouard Ivanov,¹ Jose Palomo,³ Michael Rosticher,³ Sheon Chua,¹ Tristan Briant,¹ Pierre-Francois Cohadon,¹ Antoine Heidmann,¹ Thibaut Jacqmin,¹ and Samuel Deléglise¹

¹*Laboratoire Kastler Brossel, Sorbonne Université, CNRS, ENS-Université PSL, Collège de France, 75005 Paris, France*

²*Département de Physique, ENS-Université PSL, CNRS, 24 rue Lhomond, F-75005 Paris, France*

³*Laboratoire Pierre Aigrain, ENS-Université PSL, Sorbonne Université, CNRS, 24 rue Lhomond, 75231 Paris, France*

(Dated: December 3, 2024)

While the main loss channel of planar microwave superconducting resonators has been identified to be related to an external coupling to a two-level system bath, the behavior of such a cavity in an environment strongly pumped by a detuned tone has yet to be fully understood. Here, a semi-classical theoretical model describing the interaction of such resonators with the Two-Level Systems is derived, to which experimental datas obtained with different substrate materials are fitted. Performing the experiments with different substrates allows the tailoring of fundamental properties of the interacting two-level system bath.

Microwave superconducting resonators are an ubiquitous resource in various quantum devices, ranging from kinetic inductance bolometers [1, 2], parametric amplifiers [3, 4], and embedded circuits for cavity quantum electrodynamics [5–7]. In addition, they play a central role as a microwave interface for various hybrid quantum systems such as solid-state spins [8], mechanical resonators [9, 10], and ferromagnetic magnons [11, 12]. Owing to the very low resistivity of superconducting materials, combined with advanced electromagnetic engineering of radiation losses, the dominant loss channel of such resonators is the dielectric losses due to the presence of a two-level system (TLS) bath in amorphous materials [13, 14]. Due to the non-linear nature of the TLS, this loss channel is found to be dependent on the resonator occupancy, originating from thermal fluctuations [15], from resonant excitation [16, 17] or from non-degenerate resonant mode occupancy [18, 19]. Moreover, an increasing effort has been devoted to the characterization of the microscopic properties of individual TLS probed under stress [20] or DC voltage bias [21]. However, in many cases, strong microwave tones are applied with significant frequency detuning with respect to the resonance frequency [22, 23] in order to activate a parametric interaction between the resonator mode and another degree of freedom. In this configuration, the off-resonant microwave tone responsible for the saturation of the TLS bath is spectrally distinct from the resonant mode subjected to the losses, giving simultaneous rise to a shift of the resonance frequency and a modification of the population dependency of the quality factor.

In this letter, we derive a semi-classical model that accounts for the energy relaxation properties of a microwave resonator due to the presence of an off-resonance pumped TLS bath. This model reproduces the experimental characterizations conducted on lumped-element

coplanar resonators fabricated on various substrates. From these measurements, the model allows the extraction of the average spectral distribution of the TLS, as well as the relaxation properties and typical coupling rate to the resonator. This study covers a wide range of experimental situations as of yet unexplored. Due to the rapid rise of hybrid quantum circuits, it is anticipated that the model and methodology will be widely applicable in the design and characterization of superconducting resonators, and provides a new tool for the investigation of the spectral structure of amorphous materials.

In this work, we study lumped-element resonators, in which an interdigitated capacitor and a meander inductor are connected in parallel. This geometry was optimized to maximize the coupling of the microwave mode to an external degree-of-freedom such as localized emitters [24, 25] or the motion of a planar dielectric membrane placed in the evanescent field of the electrodes via dielectric gradient forces [26]. A good approximation of the electrostatic potential in the vicinity of the interdigitated capacitor is given by the harmonic approximation [27]

$$V(x, z) = V_0 \sin(2\pi x/a) e^{-2\pi|z|/a}, \quad (1)$$

where a is the period of the electrodes oriented along the y -axis and interleaved along the x -axis. This shows that the nominal extent of the electrostatic potential is inversely proportional to the period, and that the electrostatic energy can thus be confined in an arbitrarily small region around the electrode plane $z = 0$ by reducing a . This confinement is advantageous in the context of hybrid quantum circuits, where coupling of an electromagnetic mode to a well-controlled additional system is desirable. However, this makes the resonator highly sen-

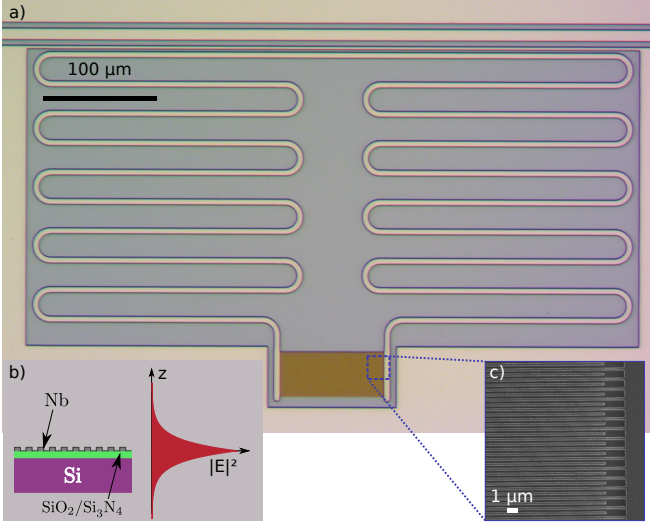


FIG. 1. a) Optical micrograph of the microwave cavity. b) The dielectric environment of the capacitance (left) and the profile of the electric field generated (right). Silicon is represented in purple, niobium is represented in grey, and the optional amorphous dielectric layer is represented in green. c) zoom on the capacitor using electron microscopy.

sitive to surface defects located at the various interfaces between superconducting material, substrate, and vacuum. The interaction with these defects, described by the coupling to a TLS bath, is the dominant source of dissipation in planar resonators [28] and constitutes the main subject of this article. We have fabricated such lumped-element resonators with a small interdigitated electrode period $a = 1 \mu\text{m}$ to confine the field in a layer of thickness $\sim 200 \text{ nm}$ around the electrode plane.

Fig. 1 shows an optical micrograph of such a resonator. The meander, of length $l \sim 5 \text{ mm}$, creates an inductance $L \approx \mu_0 l$ in the 5 nH range. In addition, as a consequence of Eq. (1), the capacitance of the interdigitated capacitor is given by (see supplementary material)

$$C = S\epsilon_0(1 + \epsilon_s)/a, \quad (2)$$

where S is the area of the interdigitated electrodes and ϵ_s is the relative permittivity of the substrate below the electrodes. We have chosen S such that $C \sim 0.12 \text{ fF}$, resulting in a resonance frequency $\omega_c/2\pi = 1/2\pi\sqrt{LC} \approx 6 \text{ GHz}$. Finally, the resonator is probed by a feedline with an inductive coupling rate $\Gamma_{\text{ext}}/2\pi \approx 0.2 \text{ MHz}$.

To probe the influence of the TLS bath on the resonator, we have performed a pump-probe experiment: a strong pump, detuned by several linewidths from the cavity resonance, saturates the TLS bath and a weak probe is used to measure the resonance frequency $\omega_c/2\pi$ and full damping $\Gamma/2\pi$ of the resonator (See Figure 2). These quantities are extracted from the probe transmission spectrum \mathcal{T} (see Figure 2c) using a fit formula that properly takes into account the effect of standing waves

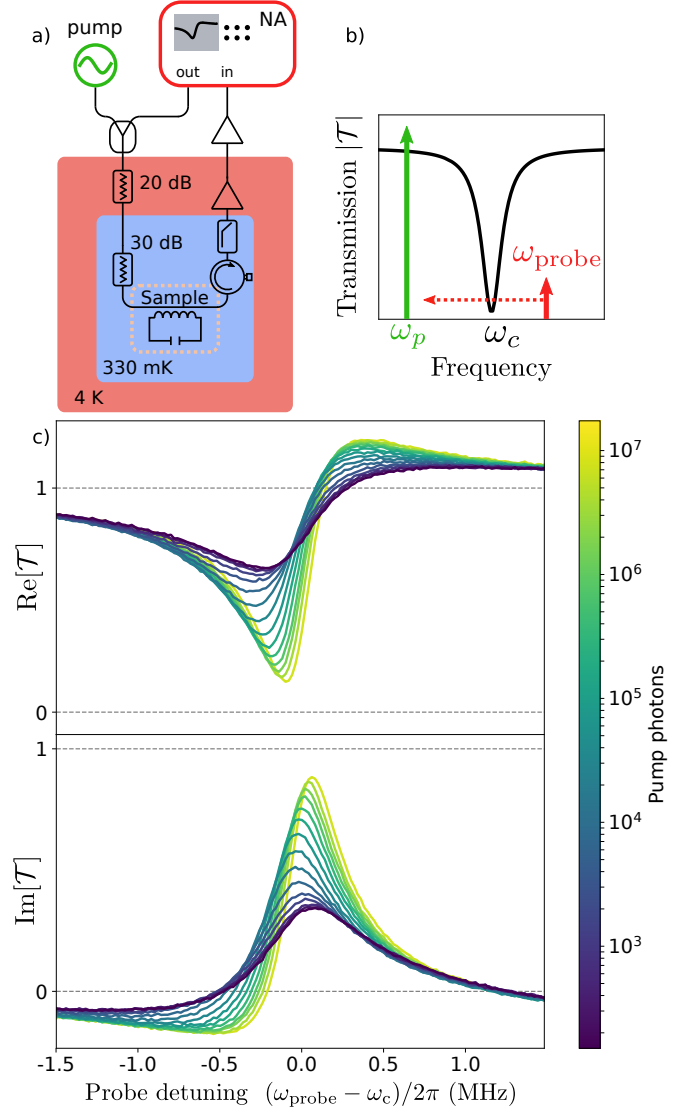


FIG. 2. a) Experimental setup. b) Experimental protocol: a strong pump field is applied far-detuned from a microwave cavity resonance, while a weak probe field is swept across the cavity resonance to measure its transmission spectrum \mathcal{T} . c) Real (top) and imaginary part (bottom) of the transmission for various intracavity photon numbers.

in the coupling waveguide [28]. Notably, this procedure allows to precisely extract the internal losses Γ_i from the total cavity linewidth $\Gamma = \Gamma_i + \Gamma_{\text{ext}}$. While the weak probe has a negligible effect on the TLS bath, the pump affects the population imbalance $\langle \sigma_z(\omega_q) \rangle$ according to the saturation law for a TLS at frequency ω_q

$$\langle \sigma_z \rangle = \langle \sigma_z \rangle_{\text{th}} \left(1 - \frac{\Gamma_2^2 C}{(\omega_q - \omega_p)^2 + \Gamma_2^2 (1 + C)} \right), \quad (3)$$

where $\langle \sigma_z \rangle_{\text{th}} = -\tanh(\hbar\omega_q/2k_B T) \approx -0.52$ is the thermal imbalance resulting from the Fermi-Dirac distribution at the base temperature $T = 330 \text{ mK}$ of our ^3He cryostat, Γ_2 (Γ_1) the TLS dephasing (energy relaxation)

rate, $\mathcal{C} = 4ng^2/\Gamma_1\Gamma_2$ the cooperativity of the TLS given the coupling rate g , and the number of pump intracavity photons n at the angular frequency ω_p . In turn, the population difference $\langle\sigma_z(\omega_q)\rangle$ of a single TLS induces a shift of the complex cavity frequency [19]

$$\delta\omega = \frac{g^2\langle\sigma_z(\omega_q)\rangle}{\omega_q - \omega_c + i\Gamma_2}. \quad (4)$$

The frequency shift and damping, as measured by the probe beam, are related to the real and imaginary parts of $\delta\omega$. The total frequency shift and damping are obtained by integrating the contribution of individual TLS, assuming a flat spectral distribution of density P_0 , uniform coupling rate g , and no interaction between individual TLSs, leading to (see supplementary material)

$$\Delta\omega_c = -\frac{P_0g^2\langle\sigma_z\rangle_{\text{th}}}{2} \frac{\mathcal{C}}{\sqrt{1+\mathcal{C}}} \frac{\delta}{\delta^2 + (1 + \sqrt{1+\mathcal{C}})^2}, \quad (5)$$

$$\Gamma_c = -P_0g^2\langle\sigma_z\rangle_{\text{th}} \left[1 - \frac{\mathcal{C}}{\sqrt{1+\mathcal{C}}} \frac{1 + \sqrt{1+\mathcal{C}}}{\delta^2 + (1 + \sqrt{1+\mathcal{C}})^2} \right]. \quad (6)$$

In these formulas, $\delta = (\omega_p - \omega_c)/\Gamma_2$ is the normalized pump detuning with respect to the resonator frequency. In particular, the limiting case $\delta = 0$ describes the result of single-tone experiments where the probe tone itself is responsible for the TLS-bath saturation. In this case, $\Delta\omega_c = 0$ and Γ_c monotonically decreases towards 0 as \mathcal{C} tends to infinity. In contrast, the detuned pump experiment gives rise to a rich set of predictions: while the monotonous decrease of Γ_c is barely modified, a non-zero frequency shift $\Delta\omega_c$ is predicted for intermediate values of \mathcal{C} . The physical interpretation of this phenomenon is illustrated in Figure 3c (3d) showing the ground state population as a function of TLS frequency for a positive (negative) pump detuning $\Delta = \omega_p - \omega_c$ and various pump powers. At low pump power $\mathcal{C} \ll 1$, the TLS transition is not saturated, such that only the TLS resonant with the pump ($|\omega_q - \omega_p| < \Gamma_2$) are excited. The corresponding depletion in ground-state population, increasing with \mathcal{C} , gives rise to a frequency pull of the cavity frequency towards the pump frequency, as predicted by Eq. 4. On the other hand, in the limit of a saturated transition $\mathcal{C} \gg 1$, the width of the depletion in ground state population $\Gamma_2\sqrt{1+\mathcal{C}}$ can exceed the pump-cavity detuning Δ , such that the asymmetry of the ground-state population with respect to ω_c vanishes, hence, $\Delta\omega_c$ also tends to 0 for $\mathcal{C} \gg 1$.

The combined dependence of $\Delta\omega_c$ and Γ_c as a function of pump detuning and pump power can be used to separately extract the TLS spectral density P_0 , their coupling to the resonator mode characterized by the coupling rate g , and their relaxation rate Γ_2 . In the following, we assume $\Gamma_1 = 2\Gamma_2$ as the dependence over Γ_1 cannot be resolved independently using Eqs. (5) and (6).

To validate the method, measurements have been performed on different resonators, fabricated on 3 different samples that are expected to yield very distinct TLS populations near the substrate interface:

- (Si) A 250 μm substrate of FZ grown (100) intrinsic silicon, with a resistivity of more than 10 000 $\Omega\cdot\text{cm}$,
- (Si/SiO₂) 500 μm of FZ grown (100) P-doped type-n silicon, with a resistivity of more than 10 000 $\Omega\cdot\text{cm}$, with 2 μm of SiO₂ from thermal oxidation,
- (Si/SiN) 650 μm of CZ grown (100) silicon, with P/Boron doping and a resistivity of 1-30 $\Omega\cdot\text{cm}$, with 200 nm of Si₃N₄ deposited through LPCVD.

In every case, 10 nearly identical resonators are realized by electron-beam lithography on a 100 nm thick niobium layer evaporated using a Plassys evaporator under ultra-high vacuum ($\approx 5 \times 10^{-10}$ mbar). The resonators have been multiplexed on the same coupling waveguide and their resonance frequency was staggered by incrementing the capacitor's area by steps of $\sim 2.5\%$. 6 resonances out of 10 have been observed for the Si substrate, 4 for the Si/Si₃N₄ substrate, and 3 for the Si/SiO₂ substrate. The missing resonances are attributed to short circuits between the interdigitated electrodes of the resonator.

To experimentally extract the model parameters, the frequency shift $\Delta\omega_c$ and intrinsic damping Γ_i are measured systematically for various intracavity pump photon numbers n_j and detunings Δ_j , for $j \in \{0, N_{\text{meas}}\}$ using the setup in Figure 2. An example of such a measurement is given in Figure 3, together with a fit using Eqs. 5 and 6. In addition to P_0 , g , and Γ_2 , the only free parameters are Γ_∞ , an additive source of loss unrelated to the TLS bath ($\Gamma_i = \Gamma_c + \Gamma_\infty$), and the natural frequency of the resonator ω_c . Despite the small number of fit parameters the agreement between theory and experiment is excellent, which justifies *a posteriori* the assumptions of our model. The error bars on the various parameters are calculated by a bootstrap method: a random subsample of the data points $\{\Delta\omega_c(n_i, \Delta_i), \Gamma_c(n_i, \Delta_i)\}_{i \in [0..N_{\text{meas}}]}$ is chosen for parameter estimation (the number of points in the subsample is equal to the number of measurements N_{meas} , however multiple identical datapoints are not excluded). The operation is repeated 1000 times to determine measurement mean value and standard deviation.

The extracted parameters for the three types of resonators are listed in Table I, together with a 95% confidence interval. As foreseen, the samples that are realized on a bare silicon substrate, which should contain very few TLS defects, since no macroscopic oxidation has been performed, have the smallest TLS damping. This is characterized by the value $\Gamma_c^0 = P_0g^2$, which corresponds to the total TLS damping extrapolated at 0-temperature, and 0-pump power. We find an average value of $\langle\Gamma_c^0\rangle = 2\pi \times 0.33$ MHz for Si resonators,

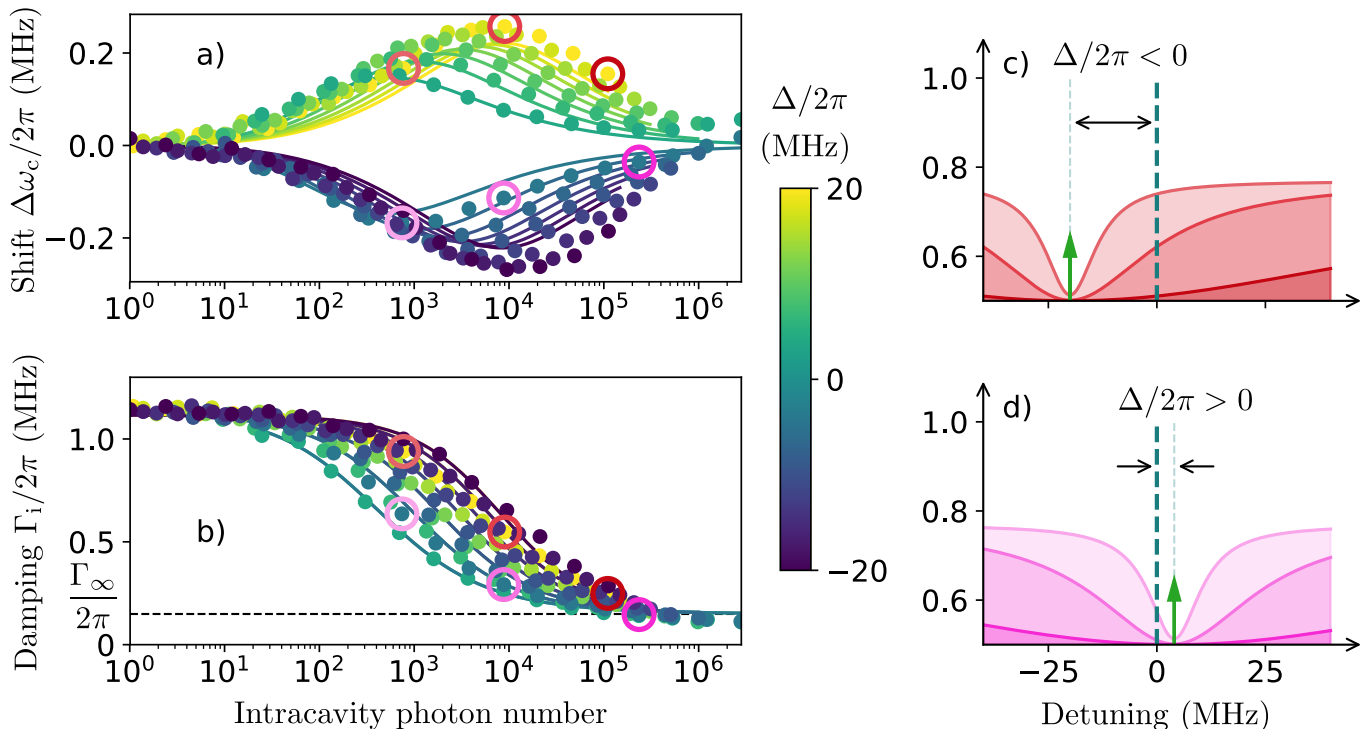


FIG. 3. (a) Shift of the cavity frequency and (b) damping of the resonator, versus the number of intracavity photons. Each color corresponds to a different detuning. Points correspond to experimental data, while solid lines correspond to fits from the model. (c) and (d) are computed ground state population distribution of the two-level systems versus the frequency detuning $\omega_q - \omega_c$, respectively for the red-circled and pink-circled points in (a) and (b). This measurement was performed on the sample Si/SiO₂, with $\omega_c/2\pi = 7.521$ GHz (see table I).

$2\pi \times 1.2$ MHz for Si/Si₃N₄ resonators and $2\pi \times 1.5$ MHz for Si/SiO₂ respectively. As apparent on the confidence intervals, this parameter is very well estimated by the model. Indeed, it directly relates to the measured damping at low pump power. The individual extraction of P_0 and g is made possible by fitting the shape of $\Delta\omega_c$ and Γ_i , albeit with a smaller confidence interval. For Si/SiO₂ samples, the larger damping is clearly explained by a larger TLS spectral density $\langle P_0 \rangle \sim 4.4$ times larger than for Si samples. On the other hand, surprisingly, Si/Si₃N₄ resonators have a TLS spectral density comparable to that of Si resonators, but individual TLS couplings $\langle g \rangle \sim 2.2$ times larger, probably originating from the strong overlap between the electric field profile and the 200 nm amorphous layer. The sometimes quite big variability of the extracted parameters between similar samples can be explained by the fact that the number of TLSs effectively interacting with the resonator can be approximated by $n_{\text{TLS}} = P_0\Gamma_2/2\pi \sim 4.1$, which is rather small. Finally, let's note that the average coupling g determined in this work is approximately a factor 4 larger than previously reported in planar resonators fabricated on Si substrates [19]. This is likely a consequence of the sub-micron confinement of the electric field in our interdigitated capacitors.

In conclusion, we have presented an experimental

method to characterize the non-linear properties of TLS bath. The method has been applied to lumped-element resonators that have been specifically optimized to confine the electric field in a small region around the substrate surface. By selectively saturating a fraction of the TLSs that is resonant with a strong detuned-pump field, and simultaneously measuring the cavity spectrum with a weak probe field, we have observed clear signatures of the interaction with the non-linear bath. The details of the evolution of the resonance frequency and damping as a function of the pump detuning can be used to infer physical properties of the bath, such as the spectral density of TLS, their coupling to the resonator, and their lifetime. The prerequisite of this technique boils down to standard microwave equipment and constitutes a useful tool to precisely characterize the properties of TLS bath - the dominant loss channel of planar superconducting resonators. Furthermore, the physical situation considered here is ubiquitous in parametrically coupled systems where a particular interaction is activated by a strong pump-field detuned with respect to the resonant mode frequency. In this regime, the coupled dynamic of the resonant mode and TLS bath has to be carefully studied since pump-photons can be scattered to the resonator via the interaction with TLSs, leading to an effective heating process. This phenomenon is currently under theoretical

Type of wafer	$\Gamma_c^0/2\pi$ (kHz)	$g/2\pi$ (kHz)	P_0 (MHz $^{-1}$)	$\Gamma_1/2\pi$ (kHz)	$\omega_c/2\pi$ (GHz)
Si/Si ₃ N ₄	2000 ± 73	540 ± 98	1.1 ± 0.4	3400 ± 1000	6.037
Si/Si ₃ N ₄	1200 ± 86	510 ± 90	0.79 ± 0.31	3500 ± 1400	5.958
Si/Si ₃ N ₄	620 ± 69	440 ± 170	0.56 ± 0.4	4300 ± 2200	5.886
Si/Si ₃ N ₄	790 ± 90	240 ± 59	2.3 ± 1.4	5300 ± 2500	5.742
Si	300 ± 22	200 ± 60	1.3 ± 0.39	2200 ± 820	5.069
Si	300 ± 22	170 ± 43	1.8 ± 0.52	2200 ± 710	5.300
Si	330 ± 19	200 ± 44	1.3 ± 0.36	2400 ± 790	5.378
Si	330 ± 22	150 ± 27	2.3 ± 0.54	2500 ± 710	5.229
Si	280 ± 23	160 ± 44	1.8 ± 0.57	2300 ± 800	5.114
Si	410 ± 24	220 ± 37	1.4 ± 0.41	1000 ± 840	5.443
Si/SiO ₂	1400 ± 28	380 ± 33	1.5 ± 0.25	2700 ± 870	7.657
Si/SiO ₂	1900 ± 50	170 ± 10	11 ± 1.4	2800 ± 440	7.521
Si/SiO ₂	1300 ± 18	150 ± 11	10 ± 1.4	1300 ± 440	7.109

TABLE I. Extracted parameters of the TLS bath for the three types of substrate

investigation [29] and its characterization, which requires a quantum limited read-out to resolve the associated fluctuations, will be the subject of future work.

The authors would like to thank Paolo Forni and Alain Sarlette for insightful discussions, Takis Kontos for his help with the Niobium deposition facility, Sundae Chen, Leo Morel and Leonhard Neuhaus for early developments. This work was supported by a starting grant from "Agence Nationale pour la Recherche" QuNaT (ANR-14-CE26-0002). E.F. is funded by a Junior research chair from the LabEX ENS-ICFP: ANR-10-LABX-0010/ANR-10-IDEX-0001-02 PSL*. E.I. acknowledges support from the European Unions Horizon 2020 Programme for Research and Innovation under grant agreement No. 722923 (Marie Curie ETN - OMT). S. C. is supported by the grant ANR ExSqueez (ANR-15-CE30-0014).

- [1] J. Sauvageau and D. Macdonald, IEEE Transactions on magnetics **25**, 1331 (1989).
- [2] M. D. Audley, R. L. Kelley, and G. L. Rawley, Journal of Low temperature physics **93**, 245 (1993).
- [3] A. Roy and M. Devoret, Comptes Rendus Physique **17**, 740 (2016).
- [4] J.-D. Pillet, E. Flurin, F. Mallet, and B. Huard, Applied Physics Letters **106**, 222603 (2015).
- [5] A. Blais, R.-S. Huang, A. Wallraff, S. M. Girvin, and R. J. Schoelkopf, Physical Review A **69**, 062320 (2004).
- [6] I. Rau, G. Johansson, and A. Shnirman, Physical Review B **70**, 054521 (2004).
- [7] A. Wallraff, D. Schuster, A. Blais, L. Frunzio, R.-S. Huang, J. Majer, S. Kumar, S. Girvin, and R. Schoelkopf, Nature **461**, 162 (2004).
- [8] A. Andr, D. DeMille, J. M. Doyle, M. D. Lukin, S. E. Maxwell, P. Rabl, R. J. Schoelkopf, and P. Zoller, Nature Physics **2**, 636 (2006).
- [9] J. Teufel, T. Donner, L. Dale, J. Harlow, M. S. Allman, K. Cicak, A. J. Sirois, J. D. Whittaker, K. W. Lehnert, and R. W. Simmonds, Nature **475**, 359 (2011).
- [10] L. Tth, N. R. Bernier, A. Nunnenkamp, A. K. Feofanov, and T. J. Kippenberg, Nature **13**, 783 (2017).
- [11] Y. Tabuchi, S. Ishino, T. Ishikawa, R. Yamazaki, K. Usami, and Y. Nakamura, Physical Review Letter **113**, 083603 (2014).
- [12] Y. Tabuchi, S. Ishino, A. Noguchi, T. Ishikawa, R. Yamazaki, K. Usami, and Y. Nakamura, Science (2015), 10.1126/science.aaa3693.
- [13] H. Wang, M. Hofheinz, J. Wenner, M. Ansmann, R. C. Bialczak, M. Lenander, E. Lucero, M. Neeley, A. D. OConnell, D. Sank, M. Weides, A. N. Cleland, and J. M. Martinis, Applied Physics Letters **95**, 233508 (2009).
- [14] R. Barends, H. L. Hortensius, T. Zijlstra, J. J. A. Baselmans, S. J. C. Yates, J. R. Gao, and T. M. Klapwijk, Applied Physics Letters **92**, 223502 (2008).
- [15] J. Gao, M. Daal, J. M. Martinis, A. Vayonakis, J. Zmuidzinas, B. Sadoulet, B. A. Mazin, P. K. Day, and H. G. Leduc, Applied Physics Letters **92**, 212504 (2008).
- [16] T. Lindström, J. E. Healey, M. S. Colclough, C. M. Muirhead, and A. Y. Tzalenchuk, Physical Review B **80**, 132501 (2009).
- [17] S. T. Skacel, C. Kaiser, S. Wuensch, H. Rotzinger, A. Lukashenko, M. Jerger, G. Weiss, M. Siegel, and A. V. Ustinov, Applied Physics Letters **106**, 022603 (2015).
- [18] J. M. Sage, V. Bolkhovsky, W. D. Oliver, B. Turek, and P. B. Welander, Journal of Applied Physics **109**, 063915 (2011).
- [19] N. Kirsh, E. Svetitsky, A. L. Burin, M. Schechter, and N. Katz, Physical Review Materials **1**, 012601 (2017).
- [20] J. Lisenfeld, G. J. Grabovskij, C. Müller, J. H. Cole, G. Weiss, and A. V. Ustinov, Nature communications **6**, 6182 (2015).
- [21] B. Sarabi, A. N. Ramanayaka, A. L. Burin, F. C. Wellstood, and K. D. Osborn, Physical Review Letters **116**, 167002 (2016).
- [22] C. Regal, J. Teufel, and K. Lehnert, Nature Physics **4**, 555 (2008).
- [23] T. Rocheleau, T. Ndukum, C. Macklin, J. B. Hertzberg, A. A. Clerck, and K. C. Schwab, Nature **463**, 72 (2010).
- [24] T. Douce, M. Stern, N. Zagury, P. Bertet, and P. Milman, Physical Review A **92**, 052335 (2015).
- [25] P. Haikka, Y. Kubo, A. Bienfait, P. Bertet, and K. Mølmer, Physical Review A **95**, 022306 (2017).
- [26] Q. P. Unterreithmeier, E. M. Weig, and J. P. Kotthaus, Nature **458**, 1001 (2009).

- [27] M. Den Otter, *Sensors and Actuators, A* **96**, 140 (2002).
- [28] K. Geerlings, S. Shankar, E. Edwards, L. Frunzio, R. J. Schoelkopf, and M. H. Devoret, *Applied Physics Letters* **100**, 192601 (2012).
- [29] P. Forni, A. Sarlette, T. Capelle, E. Flurin, S. Delglise, and P. Rouchon, (2018), arXiv:1803.07810 [quant-ph].

Supplementary material: energy relaxation properties of a microwave resonator coupled to a pumped two-level system bath

Thibault Capelle,¹ Emmanuel Flurin,² Edouard Ivanov,¹ Jose Palomo,³ Michael Rosticher,³ Sheon Chua,¹ Tristan Briant,¹ Pierre-Francois Cohadon,¹ Antoine Heidmann,¹ Thibaut Jacqmin,¹ and Samuel Deléglise¹

¹Laboratoire Kastler Brossel, Sorbonne Université, CNRS, ENS-Université PSL, Collège de France, 75005 Paris, France

²Département de Physique, ENS-Université PSL, CNRS, 24 rue Lhomond, F-75005 Paris, France

³Laboratoire Pierre Aigrain, ENS-Université PSL, Sorbonne Université, CNRS, 24 rue Lhomond, 75231 Paris, France

(Dated: December 3, 2024)

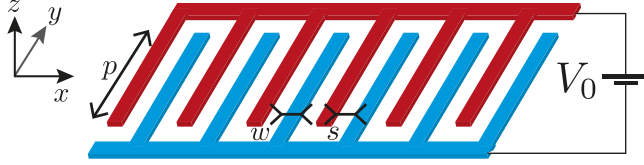


FIG. 1. Schematic of an interdigitated capacitor

ELECTRIC FIELD LOCALIZATION IN LUMPED-ELEMENT RESONATORS

We use the schematic of Figure 1 to describe the geometry of the interdigitated capacitor: since the electrodes contain a large number of teeth, we assume an infinite periodic system in the x direction, with a period $a = 2(s+w)$. Further, as the length p of the teeth is much larger than their period a , the field is therefore assumed to be invariant along the y direction.

For a given static voltage difference V_0 across the electrodes, a potential $V(x, z)$ that fulfills the Laplace equation:

$$\Delta V = 0 \quad (1)$$

needs to be found. In both half spaces ($z > 0$ and $z < 0$). Moreover, in the plane $z = 0$, the potential should be uniform on the electrodes:

$$\begin{cases} V(x, 0) = V_0/2 & \text{for } x \in [s/2, s/2 + w] \\ V(x, 0) = -V_0/2 & \text{for } x \in [-s/2 - w, -s/2], \end{cases} \quad (2)$$

and the charge distribution

$$\sigma(x, 0) = \epsilon_0 \left(\left. \frac{dV}{dz} \right|_{z=0^+} - \epsilon_s \left. \frac{dV}{dz} \right|_{z=0^-} \right) \quad (3)$$

should be zero outside the electrodes. The solution $V(x, z)$ can be developed as a Fourier series:

$$V(x, z) = \sum_{n \in \mathbb{N}^*} \sin\left(\frac{2\pi n x}{a}\right) V_n(z).$$

Substituting into Eq. 1, we get the differential equation:

$$\frac{d^2 V_n}{dz^2}(x, z) = \left(\frac{2\pi n}{a}\right)^2 V_n(x, z).$$

Finally, since the potential is continuous in $z = 0$, and the solutions diverging for $|z| \rightarrow \infty$ can be discarded, we obtain:

$$V(x, z) = \sum_{n \in \mathbb{N}^*} B_n \sin\left(\frac{2\pi n x}{a}\right) e^{-\frac{2\pi n}{a}|z|}, \quad (4)$$

where $\{B_n\}_{n \in \mathbb{N}^*}$ are a discrete set of constants of integration to be determined using the limit conditions given by Eq. 2 and 3. A good analytical approximation of the coefficients B_n is given in ref. [1]. However, for $w \approx s$, we find that the first term of the series contains $\sim 92\%$ of the stored electrostatic energy, and as such, a good approximation of the capacitance can be obtained by truncating the series to first order:

$$V(x, y) = V_0/2 \sin\left(\frac{2\pi x}{a}\right) e^{-\frac{2\pi}{a}|z|}. \quad (5)$$

This shows that the field $E = -\nabla V$ is confined in a layer of height $\sim a/2\pi$ around the electrode plane. In particular, this confinement can be arbitrarily increased by reducing the period a of the interdigitated capacitor. By substituting Eq. 5 into Eq. 3, we get:

$$\sigma = \epsilon_0 V_0 \frac{2\pi}{a} \sin\left(\frac{2\pi x}{a}\right). \quad (6)$$

From Eq. 5 and 6, it is evident that the truncated Fourier series in Eq. 4 doesn't perfectly fulfill Eq. 2 and 3 conditions. However, the capacitance C can be well-approximated by taking the ratio:

$$C = N_{\text{pairs}} \frac{q}{V_0}, \quad (7)$$

where N_{pairs} is the number of tooth pairs, and

$$q = p \int_0^{a/2} \sigma(x) dx = p \epsilon_0 (1 + \epsilon_s) V_0$$

is the charge accumulated on the positive electrode. Eq (2) in the main text follows directly from Eq. 7.

EFFECT OF THE TLS BATH

We first consider the interaction of a single TLS, characterized by a transition energy $\hbar\omega_q$, and the ladder operator σ_+ , with a cavity characterized by an angular frequency ω_c and the creation operator \mathbf{a}^\dagger . Denoting g the rate of interaction, and J the drive strength, in the rotating frame (at pump frequency ω_p) the dynamics of the system is described by the Jaynes-Cummings Hamiltonian, given as:

$$H = \hbar(\omega_p - \omega_c)\mathbf{a}^\dagger\mathbf{a} + \frac{\hbar(\omega_p - \omega_q)}{2}\sigma_z + i\hbar g(\mathbf{a}^\dagger\sigma - \mathbf{a}\sigma^\dagger) + i\hbar J(\mathbf{a}^\dagger - \mathbf{a}).$$

The dissipation is described by the Lindblad equation:

$$\frac{d\rho}{dt} = -\frac{i}{\hbar}[H, \rho] + \Gamma_{\uparrow\downarrow}(n_{\text{th}} + 1)\mathcal{D}_\sigma(\rho) + \frac{\Gamma_\phi}{2}\mathcal{D}_{\sigma_z}(\rho) + \Gamma_{\uparrow\downarrow}n_{\text{th}}\mathcal{D}_{\sigma_+} + \Gamma_0\mathcal{D}_\mathbf{a}(\rho),$$

with $n_{\text{th}} = \frac{1}{e^{\hbar\omega/kT} - 1}$ the occupation number of the TLS, $\Gamma_0 = \Gamma_{\text{ext}} + \Gamma_\infty$ the damping of the cavity in the absence of TLS, Γ_ϕ the potential dephasing rate, $\Gamma_{\uparrow\downarrow}$ the energy loss rate at zero temperature, and:

$$\mathcal{D}_A(\rho) = A\rho A^\dagger - \frac{1}{2}(A^\dagger A\rho + \rho A^\dagger A).$$

Using the formulas $\langle A \rangle = \text{Tr}(A\rho)$ and $\frac{d}{dt}\langle A \rangle = \text{Tr}(A\frac{d}{dt}\rho)$, one can compute the Maxwell Bloch equations:

$$\frac{d\langle a \rangle}{dt} = (-i\Delta - \frac{\kappa}{2})\langle a \rangle + g\langle \sigma \rangle + J \quad (8)$$

$$\frac{d\langle \sigma \rangle}{dt} = (-i(\omega_p - \omega_q) - \Gamma_2)\langle \sigma \rangle + g\langle a\sigma_z \rangle \quad (9)$$

$$\frac{d\langle \sigma_z \rangle}{dt} = -2g(\langle a^\dagger\sigma \rangle + \langle a\sigma^\dagger \rangle) - \Gamma_1(\langle \sigma_z \rangle - \langle \sigma_z \rangle_{\text{th}}), \quad (10)$$

where we defined $\Gamma_2 = \frac{\Gamma_{\uparrow\downarrow}}{2}(1 + 2n_{\text{th}}) + \Gamma_\phi$, $\Gamma_1 = \Gamma_{\uparrow\downarrow}(1 + 2n_{\text{th}})$, $\langle \sigma_z \rangle_{\text{th}} = -1/(1 + 2n_{\text{th}}) = -\tanh(\hbar\omega/2k_B T)$ and $\Delta = \omega_p - \omega_c$. To transform this system into a closed set of equations, we neglect the correlations and factorize the products $\langle a\sigma_z \rangle = \langle a \rangle \langle \sigma_z \rangle$, $\langle \mathbf{a}^\dagger\sigma \rangle = \langle \mathbf{a}^\dagger \rangle \langle \sigma \rangle$ and $\langle a\sigma^\dagger \rangle = \langle a \rangle \langle \sigma^\dagger \rangle$. Moreover, we decompose the mean values into semi-classical stationary and modulated components $\langle a \rangle = \alpha + \delta\alpha(t)e^{-i\Delta t}$, $\langle \sigma \rangle = \sigma_0 + \delta\sigma(t)e^{-i\Delta t}$, $\sigma_z = \sigma_{z0}$, and with $\delta\alpha(t)$ and $\delta\sigma(t)$ slowly varying complex functions. The equations for the stationary components then read:

$$0 = (-i\Delta - \kappa/2)\alpha + g\sigma_0 + J \quad (11)$$

$$0 = (-i(\omega_p - \omega_q) - \Gamma_2)\sigma_0 + g\alpha\sigma_{z0} \quad (12)$$

$$0 = -2g(\alpha^*\sigma_0 + \alpha\sigma_0^*) - \Gamma_1(\sigma_{z0} - \langle \sigma_z \rangle_{\text{th}}). \quad (13)$$

From Eq. 12, we get:

$$\sigma_0 = \frac{g\alpha\sigma_{z0}}{i(\omega_p - \omega_q) + \Gamma_2}. \quad (14)$$

and from Eq. 13, we get:

$$\sigma_{z0} = \langle \sigma_z \rangle_{\text{th}} \left(1 - \frac{\Gamma_2^2 \mathcal{C}}{(\omega_q - \omega_p)^2 + \Gamma_2^2(1 + \mathcal{C})} \right), \quad (15)$$

with $\mathcal{C} = 4g^2|\alpha|^2/\Gamma_1\Gamma_2$. We then solve for the modulated parts by adiabatically eliminating the TLS dynamic ($\dot{\delta\sigma} = 0$). From Eq. 8, we obtain:

$$\dot{\delta\alpha} = -\kappa\delta\alpha/2 + g\delta\sigma, \quad (16)$$

and from Eq. 9:

$$\delta\sigma = \frac{g^2\sigma_{z0}\delta\alpha}{-i(\omega_c - \omega_q) - \Gamma_2}. \quad (17)$$

By substituting Eq. 17 into Eq. 16, we obtain:

$$\dot{\delta\alpha} = \left(-\kappa/2 + \frac{g^2\sigma_{z0}}{-i(\omega_c - \omega_q) - \Gamma_2} \right) \delta\alpha. \quad (18)$$

Hence, the complex frequency pull is given by:

$$\delta\omega = \frac{g^2\sigma_{z0}}{(\omega_q - \omega_c) + i\Gamma_2}. \quad (19)$$

We also compute the total frequency shift and damping by summing the individual contributions of all the TLSs. If we assume a homogeneous distribution of frequencies of the TLS, with a density P_0 , we have the following:

$$\begin{aligned} \delta\omega_c &= \int_{-\infty}^{\infty} d\omega_q \frac{P_0}{2\pi} \frac{g^2\sigma_{z0}}{\omega_q - \omega_c + i\Gamma_2} \\ &= \int \langle \sigma_z \rangle_{\text{th}} \left(1 - \frac{\Gamma_2^2 \mathcal{C}}{(\omega_q - \omega_p)^2 + \Gamma_2^2(1 + \mathcal{C})} \right) \\ &\quad \times \frac{P_0 g^2}{(\omega_q - \omega_c) + i\Gamma_2} \frac{d\omega_q}{2\pi}. \end{aligned}$$

This integral can be interpreted as the convolution product:

$$\delta\omega_c(\Delta) = \langle \sigma_z \rangle_{\text{th}} P_0 g^2 \times \left[\left(1 - \frac{\Gamma_2^2 \mathcal{C}}{\omega^2 + \Gamma_2^2(1 + \mathcal{C})} \right) \otimes \frac{1}{\omega + i\Gamma_2} \right] (\Delta).$$

Using standard Fourier transforms and the convolution theorem, we derive the expression:

$$\delta\omega_c = -P_0 g^2 \langle \sigma_z \rangle_{\text{th}} / 2 \left(i + \frac{\mathcal{C}}{\sqrt{1 + \mathcal{C}}} \frac{1}{\Delta/\Gamma_2 + i(1 + \sqrt{1 + \mathcal{C}})} \right). \quad (20)$$

The real and double-imaginary parts of this expression correspond to the frequency shift and damping induced by the TLS:

$$\begin{aligned} \Delta\omega_c &= \text{Re}[\delta\omega_c] \\ &= -\frac{P_0 g^2 \langle \sigma_z \rangle_{\text{th}}}{2} \frac{\mathcal{C}}{\sqrt{1 + \mathcal{C}}} \frac{\Delta/\Gamma_2}{(\Delta/\Gamma_2)^2 + (1 + \sqrt{1 + \mathcal{C}})^2}, \end{aligned} \quad (21)$$

$$\begin{aligned} \Gamma_c &= 2\text{Im}[\delta\omega_c] \\ &= -P_0 g^2 \langle \sigma_z \rangle_{\text{th}} \left[1 - \frac{\mathcal{C}}{\sqrt{1+\mathcal{C}}} \frac{1 + \sqrt{1+\mathcal{C}}}{(\Delta/\Gamma_2)^2 + (1 + \sqrt{1+\mathcal{C}})^2} \right]. \end{aligned} \quad (22)$$

PHOTON NUMBER CALIBRATION

The intracavity photon number at cryogenic temperature can be precisely quantified with the calibration of the total attenuation required for signal thermalization. To achieve this, we performed a separate experiment shown in Fig. 2a where a temperature controlled 50 Ω -termination is placed instead of the sample. The emitted Johnson-Nyquist noise is used as a calibrated signal to extract the gain of the amplification chain G . The power spectral density measured by a spectrum analyzer depends on the temperature of the 50 Ω -resistor according to $S[\omega, T] = G(\hbar\omega_c[\exp(\frac{\hbar\omega_c}{k_B T}) - 1]^{-1} + S_{\text{amp}})$ where S_{amp} is the spectral noise density added by the amplification chain. The measured power spectral density is shown in Fig. 2b as a function of the temperature of the 50 Ω -termination, the temperature is cycled up and down with a 5 minutes thermalization time for each value. The temperature sweep enables us to separate the contribution of the Johnson-Nyquist noise from the noise added from the amplification chain. Moreover, a probe is added to track slow drift of the gain of the amplification chain during the calibration. We obtain an amplification chain gain of $G = 61.8$ dB and an added noise corresponding to $S_{\text{amp}} = k_B \times 4.4$ K in agreement with the specification of the HEMT amplifier. Assuming that the amplification chain remains unchanged with respect to the setup presented in Fig.2 a) of the main text, we are

able to extract the total attenuation of the thermalization chain of 52 dB and therefore infer the photon flux at the input of the superconducting resonator $|a_{\text{in}}|^2$. Thus, the intracavity photon number can be extracted according to the following equation:

$$\bar{n} = \frac{4\kappa_c |a_{\text{in}}|^2}{\kappa_{\text{tot}}^2 + 4\Delta^2}, \quad (23)$$

where the coupling rate κ_c , the total decay rate κ_{tot} and the cavity detuning Δ are extracted from experimental data presented in Fig.2c) of the main text.

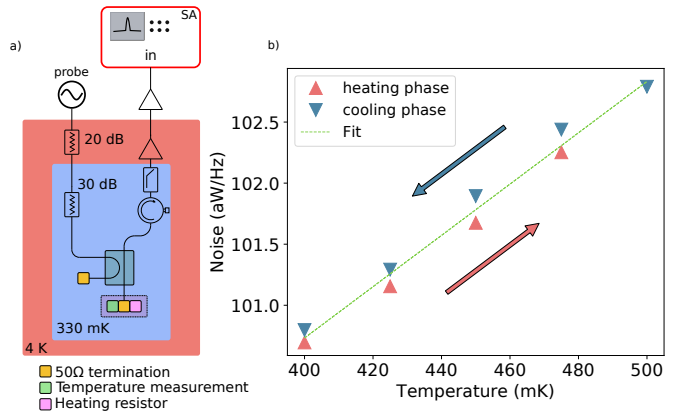


FIG. 2. (a) Setup used for the calibration of the amplification and attenuation chain. (b) Experimental results, for increasing and decreasing temperatures, with added fit.

[1] M. Den Otter, Sensors and Actuators, A **96**, 140 (2002).